Rotorcraft Hard Landing Mitigation Using Robotic Landing Gear

J. Kiefer
Guggenheim School of Aerospace Engineering,
Georgia Institute of Technology,
Atlanta, GA 30332-0150

M. Ward
Guggenheim School of Aerospace Engineering,
Georgia Institute of Technology,
Atlanta, GA 30332-0150

M. Costello
David S. Lewis Professor of Autonomy,
Guggenheim School of Aerospace Engineering,
Woodruff School of Mechanical Engineering,
Georgia Institute of Technology,
Atlanta, GA 30332-0150
e-mail: mark.costello@gatech.edu

A unique, beneficial feature of rotorcraft is their flexibility in aircraft-to-ground interfacing. For a variety of reasons, hard landings can occur when the descent rate of the aircraft is larger than intended. The resulting impact can result in vehicle damage, structural failure, injuries, etc. To reduce these risks, an attractive solution is the implementation of a robotic legged landing gear (RLLG) system. The system softens a hard landing by acting as a shock absorber with a relatively large stroke, allowing the aircraft to decelerate over a much larger distance compared with a tradition landing gear system. This paper explores the mitigation of rotorcraft hard landings via RLLG through a comprehensive multibody dynamics simulation tool. The purpose of this study is to demonstrate the efficacy of the RLLG as a robust solution to reduce loads during hard landings for multiple landing configurations. The results show that when using RLLG in place of conventional landing gear, peak loads are reduced by approximately 70–90%, depending on the landing conditions. Through Monte Carlo simulation, robotic landing gear system performance is shown to be robust to uncertain conditions. [DOI: 10.1115/1.4032286]

1 Introduction

Rotorcraft is an invaluable air vehicle for accessing remote areas that are difficult or impossible to reach by other means. A unique feature of rotorcraft is their inherent flexibility in aircraft-to-ground interfacing, including complex terrain. However, landing in uncertain conditions in stressful scenarios can lead to hard landings. A hard landing involves controlled, but relatively rapid descent of the aircraft before impacting the ground with relatively high-speed. Hard landings vary in seriousness from causing mild passenger discomfort to situations resulting in serious vehicle damage, structural failure, cargo damage, injuries, and possible loss of life. When an aircraft experiences a hard landing, it must be inspected for damage before its next flight. Hard landings are different from crash landings, which are characterized by uncontrolled descent into the ground and usually result in destruction of the vehicle. A crash landing could be considered a more severe case of a hard landing. In both cases, it is desirable for the landing gear system to minimize the loads and acceleration experienced by the aircraft.

Hard landings can occur due to several factors, including poor weather conditions, poor visibility, over-loaded aircraft, mechanical/electrical failures, and pilot error. Research has been performed to mitigate the effects of restricted visibility on the pilot's ability to operate the aircraft [1–5]. Coltman, Bolukbasi, and Laananen examined the causes of over 1000 rotorcraft crashes within a 5-yr period [6]. It was found that rotorcraft crashes and hard landings involve injuries ranging from minor to fatal, with injuries due to excessive accelerations being particularly hazardous. It has also been shown that spinal injuries are due mainly to the vertical velocity changes during impact [7]. Due to the fact that rotorcraft generally has a higher accident rate than airliners [8], crash dynamics of rotorcraft have been the subject of a significant body of literature, which lends itself to the study of hard landings. For example, several studies have found that the probability of injury and/or damage to the aircraft can be decreased through the design of hard landing mitigation technology [6–10]. Potential solutions have included the redesign of aircraft seats,

subfloor, and landing gear. Conventional landing gear design is guided by Military Standard 1290 (a), which stipulates a set of landings that the aircraft must be able to perform without substantial damage [11]. The landing gear and supporting components are sized to be sufficiently stout for these limiting hard landing cases. Additionally, conventional landing gear has been optimized for crash landings [12–17]. The skids of conventional landing gear absorb impact through plastic strain of the cross members. As such, the capability of the landing gear deteriorates over time [13]. There are also design tradeoffs when considering durability, strength, landing performance, cost, and weight. To improve on traditional skid gear, several shock absorbing methods have been considered. Some of these solutions include external, deployable airbags, collapsible honeycomb structures [18–20], collapsible metallic tubes [21], supplemental systems to be added to conventional landing gear, and other ideas [22–29]. Many of these solutions are difficult to implement, not reusable, add significant weight, and offer no additional benefits other than improved crash dynamics. An improved solution for reducing loads experienced during hard landings and crash landings is through the use of RLLG. RLLG for rotorcraft has been considered for increasing slope landing performance and decreasing pilot workload during landing leading to the ability of rotorcraft to land on unprepared landing zones with complex terrain [30].

This paper explores mitigation of rotorcraft hard landing effects by replacing conventional skid or wheel-based landing gear with an RLLG system. The mobility offered by robotic landing gear provides a means for a highly effective shock absorber with a relatively large stroke during impact. It is shown that RLLG provides a powerful and robust means to reduce loads and acceleration on the rotorcraft during hard landing events for a variety of landing conditions. Furthermore, numerous RLLG concepts are evaluated to form a clear picture of how this type of landing gear can protect rotorcraft from hard landings.

This paper begins by detailing the models and methods used in a multibody dynamic simulation tool, including descriptions the multibody simulation method, contact model, and control algorithm. The dynamic behavior of typical hard landings is then described in terms of an example rotorcraft for multiple landing conditions and landing gear configurations. Finally, the results of parametric trade studies and Monte Carlo simulations are presented, detailing the increased performance in hard landing mitigation offered by the RLLG in multiple configurations.

2 Hard Landing Event Simulation

2.1 Landing Gear Model. The robotic landing gear configuration considered here consists of four identical legs, each with two segments. The segments are connected by hinge joints to each other and the fuselage, forming a 'hip' and "knee" joint for each leg. The joints house actuators for control of leg angles. The bottom of each lower leg segment is fitted with a rigid, round peg to provide an interface with the ground surface.

For dynamic simulation, the landing gear and aircraft system is modeled as nine rigid bodies and eight connection joints. The nine rigid bodies include each leg segment (eight total), and one body representing the fuselage, main rotor, tail rotor, etc. The eight connection joints include four joints connecting the fuselage to the upper leg segments and four joints connecting the upper and lower leg segments. Each connection consists of a pinned joint with elastic, rotational stiffness and damping in the joint. The RLLG model is illustrated in Figs. 1–3.

The robotic landing gear acts as a shock absorber during the impact of a hard landing, allowing a relatively large stroke (Fig. 4). The joint stiffness and damping in the RLLG are used to control the leg angles and stroke during impact. Unlike the RLLG, a conventional skid gear does not allow such a large deflection.

2.2 Multibody Simulation Method. A basic method used to simulate the multibody system is detailed by Leylek, Ward, and Costello [31]. An overview of the simulation method is given below. The RLLG system is modeled as nine bodies with eight connection joints, as depicted in Fig. 2. A more general system is modeled as N rigid bodies connected by M joints. Each of the joints connect two of the N bodies together. The two bodies connected are referred to as the parent and child bodies.

For the ith rigid body of the system, the dynamic equations of motion are written as

$$\dot{X}_i = F_i + G_i U \tag{1}$$

X_i is the state vector of the body, F_i represents the unconstrained dynamic equations, and $G_i U$ represents the contributions of the connection constraint forces and moments to the dynamic equations. U is a vector that contains all constraint forces and moments that arise due to bodies being connected to one another via a joint. G is a matrix that when multiplied by U creates the effect of joint reaction forces and moments in the equations of motion of body i due to bodies in the system connected to body i.

The state vector of the ith rigid body is defined as

$$X_i = \begin{bmatrix} x_i & y_i & z_i & q_{0i} & q_{1i} & q_{2i} & q_{3i} & u_i & v_i & w_i & p_i & q_i & r_i \end{bmatrix}^T \tag{2}$$

Then, the unconstrained equations of motion, F_i, can be divided into four contributing elements: translational and rotational
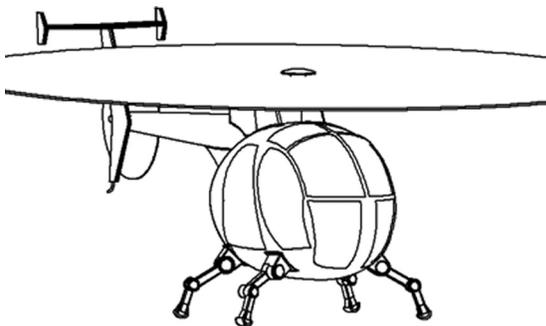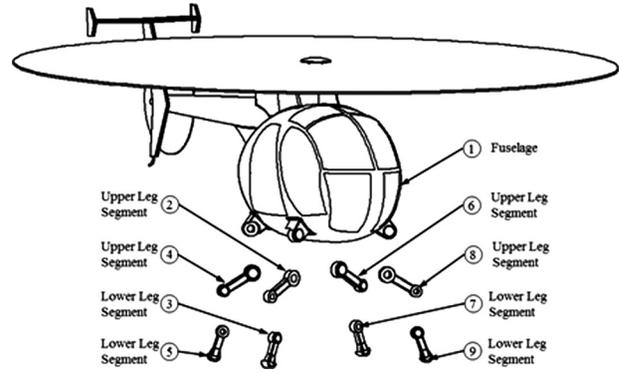
Fig. 2   Exploded view of RLLG system consisting of nine rigid bodies

kinematics, and translational and rotational dynamics. Thus, F_i can be written as

$$F_i = \begin{Bmatrix} F_{TK_i} \\ F_{RK_i} \\ F_{TD_i} \\ F_{RD_i} \end{Bmatrix} \tag{3}$$

where

$$F_{TK_i} = T_{B_i} \begin{Bmatrix} u_i \\ v_i \\ w_i \end{Bmatrix}, \quad F_{RK_i} = \frac{1}{2} \begin{bmatrix} -q_{1i} & -q_{2i} & -q_{3i} \\ q_{0i} & -q_{3i} & q_{2i} \\ q_{3i} & q_{0i} & -q_{1i} \\ -q_{2i} & q_{1i} & q_{0i} \end{bmatrix} \begin{Bmatrix} p_i \\ q_i \\ r_i \end{Bmatrix}$$

$$F_{TD_i} = \frac{1}{2} S_{\omega_i} \begin{Bmatrix} u_i \\ v_i \\ w_i \end{Bmatrix} + \frac{1}{m_i} \begin{Bmatrix} F_{X_i} \\ F_{Y_i} \\ F_{Z_i} \end{Bmatrix}, \quad F_{RD_i} = -I_i^{-1} S_{\omega_i} I_i \begin{Bmatrix} p_i \\ q_i \\ r_i \end{Bmatrix}$$

$$+ I_i^{-1} \begin{Bmatrix} M_{X_i} \\ M_{Y_i} \\ M_{Z_i} \end{Bmatrix} \tag{4}$$

$$S_{\omega_i} = \begin{bmatrix} 0 & -r_i & q_i \\ r_i & 0 & -p_i \\ -q_i & p_i & 0 \end{bmatrix} \tag{5}$$

T_{B_i} is the transformation from the ith body frame to the inertial frame, m_i and I_i are the mass and moment of inertia of the ith rigid body, and S_{ω_i} is the cross product operator for the angular rates of the ith body. The externally applied forces and moments about the mass center of the ith body do not include the effect of connection constraints. However, they can be the functions of system state and control input.

Fig. 1   RLLG system
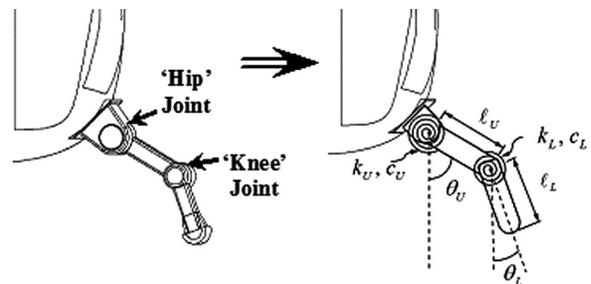
Fig. 3   Joints connecting rigid bodies are modeled as pinned joints with spring and dampers

The single body equations of motion are transformed into the multibody dynamics formulation by the addition of the G_iU term in Eq. (1). The U vector contains connection constraint forces and moments from all the connection elements of the system, not just connections associated with the ith rigid body. Then, for the jth joint, there exists nonzero G matrices for the parent and child, $G_{P,j}$ and $G_{C,j}$ that relate the effect of constraint loads on the dynamics of the connected bodies. The G_i matrices are functions of the specific connection type. To form the overall system equations, the equations represented by Eq. (1) are concatenated for all bodies

$$\dot{X} = F + GU \tag{6}$$

The matrices $G_{P,j}$ and $G_{C,j}$ are used to populate the jth block column of the G matrix. This is done for all M joints. The vector of constraint forces and moments, U, is found through constraint stabilization via nonlinear feedback control. Constraint expressions for translation and rotation are generated. For translation, the quantity of interest is the difference in the position vector from the joint point on the parent body to the joint point on the child body [31]

$$\mathbf{E}_{T_j} = \mathbf{r}_{O \to PJ} - \mathbf{r}_{O \to CJ} \tag{7}$$

For rotation, the quantity of interest is the relative rotation of the child joint frame with respect to the parent joint frame [31]

$$E_{R_j} = T_{PJ_j} T_{P_j} T_{C_j}{}^\mathrm{T} T_{CJ_j}{}^\mathrm{T} \tag{8}$$

To aid in bookkeeping the translational and rotational errors of all the joints of the system are placed into a large constraint error vector to be nulled at all times

$$E(X) = \begin{bmatrix} E_{T_1}^\mathrm{T} & E_{R_1}^\mathrm{T} & \cdots & E_{T_M}^\mathrm{T} & E_{R_M}^\mathrm{T} \end{bmatrix}^\mathrm{T} = 0 \tag{9}$$

E_{T_j} and E_{R_j} are the translational error and rotational error vectors for the jth joint, respectively. Together, Eqs. (6) and (9) represent a set of differential algebraic equations. The vector U contains all the scalar constraint forces and moments from all joints in the system, while the vector $E(X)$ contains constraint equations that must be satisfied at all times. The number of constraint equations is equal to the number of constraint force and moment scalars. Thus, E can be viewed as a system output with U acting as a control vector. Thus, we seek to find U to satisfy Eq. (9). Furthermore, if the constraint stabilization algorithm is designed to be stable and begins by satisfying the constraint equation, $E(X(t = t_0)) = 0$, the equations of motion can be numerically integrated while satisfying the constraint equations. This constraint controller is termed the "glue code controller" because it determines the constraint forces and moments that properly "glue" the system of bodies together.

a) **Free fall from rest** b) **Maximum deflection during impact** c) **Aircraft returned to static position**
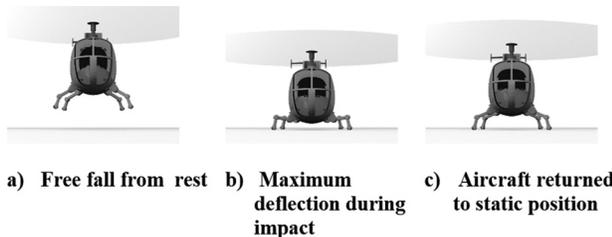
Fig. 4 Snapshots illustrating the deflection of the RLLG during a simulation. The RLLG model was also used to represent conventional gear by stiffening the system so that the deflection in (b) is much less than shown. (a) Free fall from rest, (b) maximum deflection during impact, and (c) aircraft returned to static position.

The joint errors in Eq. (9) are algebraic equations in terms of generalized coordinates. By taking a time derivative of the joint error equations, a set of algebraic equations is formed which is in terms of generalized coordinates and speeds. By taking a second time derivative of the joint errors equations, a set of differential equations is formed written in terms of generalized coordinates, generalized speeds and derivative of generalized speeds. Using the dynamic equations of motion for each body, expressions for the time derivatives of generalized speed are eliminated. Since all constraint forces and moments entering the dynamic equations enter in a linear fashion, Eq. (10) is a second-order differential equation in the joint errors that is affine in the joint constraint forces and moments [31]. The second-order dynamics for the joint constraint equations are given by

$$\ddot{E} = \tilde{F} + \tilde{G}U = 0 \tag{10}$$

where

$$\tilde{F} = \frac{\partial \dot{E}}{\partial X} F \quad \tilde{G} = \frac{\partial \dot{E}}{\partial X} G \tag{11}$$

The matrix $\tilde{G}$ is usually nonsingular, allowing direct computation of the constraint loads. Numerous methods are suitable to solve the control problem. Using feedback linearization, Eq. (10) is set equal to a pseudo control, γ

$$\ddot{E}(X) = \gamma = \tilde{F} + \tilde{G}U \tag{12}$$

The pseudo control is selected so that the constraint equation dynamics are exponentially stable. Then, the pseudo control and the constraint force and moment vector, U, are given by Eqs. (13) and (14)

$$\gamma = -2\xi\omega_n\dot{E} - \omega_n^2 E \tag{13}$$

$$U = -\tilde{G}^{-1}\left(2\xi\omega_n\dot{E} + \omega_n^2 E + \tilde{F}\right) \tag{14}$$

The damping ratio and natural frequency are chosen to stabilize the constraint error dynamic equations, which become an uncoupled set of simple damped oscillators

$$\ddot{E} + 2\xi\omega_n\dot{E} + \omega_n^2 E = 0 \tag{15}$$

This is a standard feedback linearization controller where the zero dynamics represent the dynamics of the properly coupled physical system. Elastic joints are modeled in a similar manner to the joint constraints, except that elastic joint forces and moments are simply calculated to be proportional and in an opposite direction to the joint error terms (i.e., linear springs and dampers are used).

2.3 Contact Model. During a landing event, the foot of each leg comes into contact with the ground surface. Ground contact is simulated using a soft-contact model along the lines of the model reported by Goyal et al. [32,33]. Under this model, the feet and ground plane are modeled as polyhedra. Each foot contains one vertex used to handle ground contact. Contact is evaluated at every time step of the simulation by checking for ground penetration of the vertex. If penetration has occurred, the simulation is stepped back in time to the initial contact. This usually requires interpolation between time steps. At the initial contact time, the contact model is activated. The model includes two surface elements for each contact point: one for the vertex of the foot and one for the ground plane. The surface elements define the plane of contact. They cannot penetrate each other but allow for relative in-plane motion. Parallel springs and dampers simulate contact dynamics in the normal and tangential directions of the contact plane, as shown in Fig. 5. The model allows for sliding or sticking

between the surfaces by comparing the tangential force of the springs and dampers with the static friction force, and applying the smaller of the two. The dynamics of the spring displacements are tracked and added to the state equations of the simulation

$$\dot{\vec{s}}_{1n} = \frac{c_{2n}}{c_{1n}+c_{2n}}\Delta\vec{u}_n - \frac{1}{c_{1n}+c_{2n}}\left(k_{1n}\vec{s}_{1n}+k_{2n}\vec{s}_{2n}\right) \quad (16)$$

$$\dot{\vec{s}}_{2n} = \frac{-c_{1n}}{c_{1n}+c_{2n}}\Delta\vec{u}_n - \frac{1}{c_{1n}+c_{2n}}\left(k_{1n}\vec{s}_{1n}+k_{2n}\vec{s}_{2n}\right) \quad (17)$$

$$\dot{\vec{s}}_{1t} = \frac{c_{2t}}{c_{1t}+c_{2t}}\left(\Delta\vec{u}_t - \Delta\vec{w}_t\right) - \frac{1}{c_{1t}+c_{2t}}\left(k_{1t}\vec{s}_{1t}+k_{2t}\vec{s}_{2t}\right) \quad (18)$$

$$\dot{\vec{s}}_{2t} = \frac{-c_{1t}}{c_{1t}+c_{2t}}\left(\Delta\vec{u}_t - \Delta\vec{w}_t\right) - \frac{1}{c_{1t}+c_{2t}}\left(k_{1t}\vec{s}_{1t}+k_{2t}\vec{s}_{2t}\right) \quad (19)$$

where $\vec{s}_{in}$ and $\vec{s}_{it}$ are the ith spring displacements in the normal and tangential directions, $\mathbf{u}_i$ is the absolute velocity of the contact point for the ith polyhedron, $\mathbf{w}_i$ is the absolute velocity of the surface element of the ith polyhedron, k_{in} and k_{it} are the normal and tangential spring coefficients for the ith surface element, and c_{in} and c_{it} are the normal and tangential damping coefficients for the ith surface element.

2.4 Control Algorithm. A controller is used to mitigate hard landings by commanding the torque in the hip and knee joints of the RLLG. This is accomplished by manipulating the damping and spring coefficients in the joints. The implementation of the actuation system is outside the scope of this work, but ongoing work has shown that a hydraulic or pneumatic fluid power system or geared rotational electric motors can be utilized to provide control actuation. The controller is designed as a simple state machine, building on the architecture used in Ref. [30]. A diagram of the state machine and decision tree is shown in Fig. 6. The parking brake controller was designed to level the aircraft at landing. If a leg contacts the ground, the joint stiffness zero-load point is constantly reset to the current joint deflection while the damping is set to zero. In other words, the leg is "relaxed," freely compresses as the aircraft descends, and conforms to the terrain. Once all feet are in contact, the controller state is switched to hard landing control. The hard landing control sets the joint stiffness and damping of each leg in order to minimize the peak acceleration experienced during the landing. Once the aircraft has been stopped vertically (z-velocity < 0), the joint stiffness and damping are slowly restored to nominal values to provide appropriate static clearance with the ground. During each state, there is a possibility of the legs bouncing off a rigid and lightly damped ground when the impact speed is large (especially during the "relaxed" state of the parking brake controller). To alleviate this situation, if a leg is rotating at a high rate and loses contact with the ground, the damping is set in proportion to the rotation rate. This quickly dampens the motion and brings the leg back into contact as the aircraft continues to descend. This damping control acts on top of the main parking brake and hard landing controller states.

Two options were used to implement the hard landing control. An open-loop design was used to simulate an ideal, level landing and perform trade studies. A closed-loop design was used to provide practical control for more general cases of landings. The closed-loop controller implements feedback linearization to track a constant acceleration according to the following equation:

$$\ddot{z} = u_c \quad (20)$$

The controller sets the joint stiffness and damping to achieve the vertical force associated with Eq. (20). The required joint parameters were found by assuming that the legs are massless rods (based

on their insignificant mass compared to the aircraft), and solving the resulting moment equilibrium equations

$$k_U = \frac{-f_N\left(\ell_U\sin(\theta_U)+\ell_L\sin(\theta_L)\right)-f_f\left(\ell_U\cos(\theta_U)+\ell_L\cos(\theta_L)\right)}{(\theta_U - \theta_{U,t_0})+R\dot{\theta}_U} \quad (21)$$

$$k_L = \frac{-f_N\ell_L\sin(\theta_L)-f_f\ell_L\cos(\theta_L)}{(\theta_L - \theta_{L,t_0})-(\theta_U-\theta_{U,t_0})+R(\dot{\theta}_L-\dot{\theta}_U)} \quad (22)$$

$$c_U = -R\left[\frac{f_N\left(\ell_U\sin(\theta_U)+\ell_L\sin(\theta_L)\right)+f_f\left(\ell_U\cos(\theta_U)+\ell_L\cos(\theta_L)\right)}{(\theta_U-\theta_{U,t_0})+R\dot{\theta}_U}\right] \quad (23)$$

$$c_L = -R\left[\frac{f_N\ell_L\sin(\theta_L)+f_f\ell_L\cos(\theta_L)}{(\theta_L-\theta_{L,t_0})-(\theta_U-\theta_{U,t_0})+R(\dot{\theta}_L-\dot{\theta}_U)}\right] \quad (24)$$

where f_f is the friction force with the ground, f_N is the vertical force on the leg (a function of u_c), the damping coefficients are extra parameters chosen to be proportional to the stiffness coefficients by the constant, R, and all other parameters are defined in Fig. 3.

The open-loop controller solved Eqs. (21)–(24) for a desired trajectory to create a time schedule of joint parameters to be used during the landing. The ideal trajectory of the fuselage center of mass is nearly a constant deceleration until the fuselage is brought to rest. The desired trajectory can be converted to the motion of the leg segment angles by the following geometric constraints:

$$z - \left(L_U\cos(\theta_U)+L_L\cos(\theta_L)+C\right) = 0 \quad (25)$$

$$L_U\sin(\theta_U)+L_L\sin(\theta_L)-L_U\sin(\theta_{U,t_0})-L_L\sin(\theta_{L,t_0}) = 0 \quad (26)$$

where θ_{U,t_0} and θ_{L,t_0} are the initial angles of the upper and lower leg segments, respectively (Fig. 3), and C is a constant representing the vertical distance from the fuselage mass center to the connection point of the legs. The equations were formed from the geometric constraints of a constant width between feet during the landing. The equations were differentiated and solved numerically
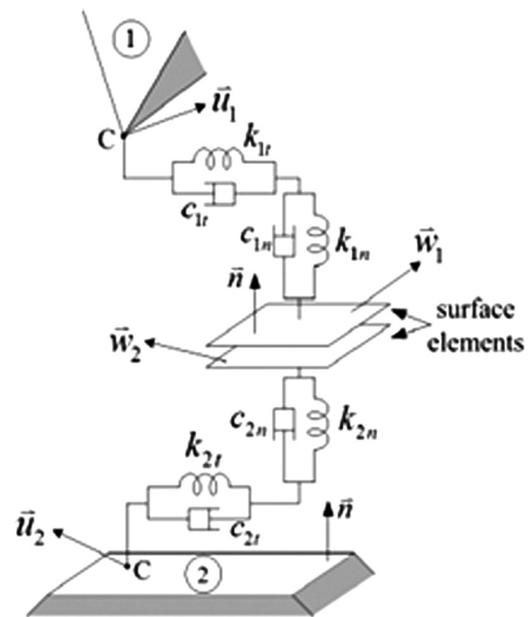
Fig. 5   Soft contact model
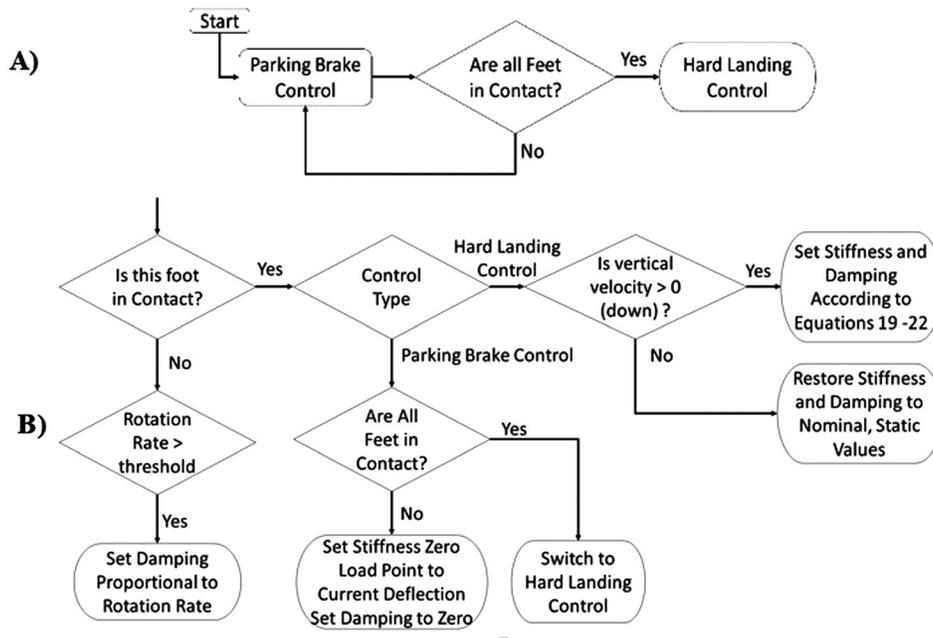
Fig. 6 Controller state machine (*a*) and detailed decision tree (*b*)

to obtain the desired trajectory of the leg segment angles and angular rates, which were used in Eqs. (21)–(24) to create the schedule of joint parameters to be followed during the landing.

3 Typical Hard Landing Dynamic Behavior

3.1 General Description of Example Rotorcraft and Landing Conditions. To underscore the landing performance of rotorcraft with an RLLG system, an OH-6A sized helicopter [34] was considered. A schematic view of the example helicopter with the RLLG is shown in Figs. 7 and 8. Ground terra mechanics were defined by setting the stiffness and damping coefficients of the contact model to large values, yielding a nearly rigid ground surface. Landing events were initiated by releasing the aircraft into free fall from a specified initial height. A hard landing is restricted to scenarios that do not result in any localized yielding in the landing gear, which limits the impact speed. The limit was estimated via finite element analysis (FEA) simulations to be about 12 ft/s
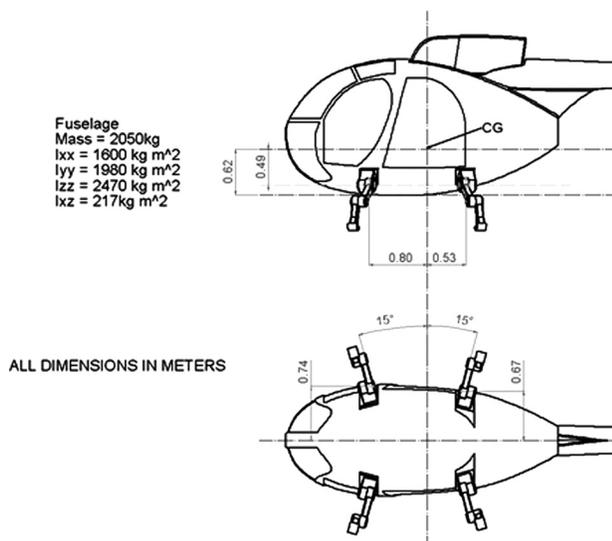
for the example helicopter with traditional skid gear. This speed is referred to as the critical speed. At larger impact speeds, yielding would occur resulting in permanent damage to traditional landing gear.

In addition to the vertical speed, other important initial conditions include the lateral and longitudinal velocity of the aircraft's mass center, the stance width of the landing gear, and the orientation of the aircraft. The stance width of the landing gear, defined by the distance between the feet of the front legs, was controlled through the initial leg angles. The initial angles define the zero-load point of the rotational springs in the leg segment joints. Larger angles provide a wider stance, which has better stability, but less stroke. The orientation was defined by specifying rotations of the aircraft about the traditional roll and pitch axes in the aircraft frame. For general orientations, initial contact may involve one or more legs.

3.2 Typical Level Hard Landing. A typical, level hard landing involves almost no rolling or pitching of the aircraft. Four phases can be identified during the landing: (1) Free fall; (2) Deceleration; (3) Recoil; and (4) Oscillation and Settling. These phases can be described by the following characteristics. During free fall, there is constant acceleration of the fuselage mass center due to gravity. During the deceleration phase, a large spike in acceleration occurs during initial contact. This corresponds to peak forces and moments on the RLLG and fuselage. The magnitude of the acceleration decreases at a rate that is largely

Fuselage
Mass = 2050kg
Ixx = 1600 kg m^2
Iyy = 1980 kg m^2
Izz = 2470 kg m^2
Ixz = 217kg m^2

ALL DIMENSIONS IN METERS

Fig. 7 Schematic of the example rotorcraft equipped with the RLLG

For Solid Aluminum,
2.7g/cm

Upper Segment
Mass = 17kg
Ixx = Iyy = 0.60 kg m^2
Izz = 0.050 kg m^2

Lower Segment
Mass = 11kg
Ixx = Iyy = 0.22 kg m^2
Izz = 0.018 kg m^2

ALL DIMENSIONS IN METERS
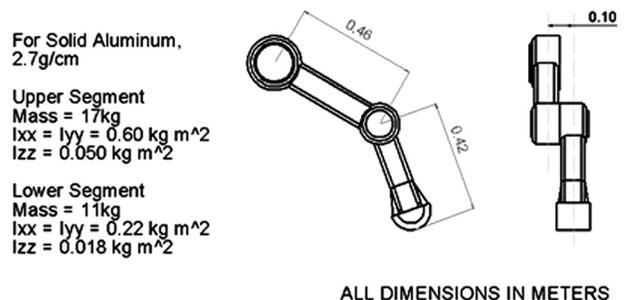
Fig. 8 Schematic of an RLLG leg

dependent on the stroke available to the RLLG. The fuselage mass center reaches a point of maximum deflection at the end of the deceleration phase. The recoil phase is entered when the stored energy in the RLLG is released and the fuselage begins to ascend. Some bouncing may occur, due in part to the nearly rigid ground. This results in additional peaks in the acceleration curve from smaller impacts. The oscillation and settling phase is entered as the fuselage mass center oscillates slightly until coming to rest at its static equilibrium position.

Snapshots of a typical hard landing simulation are shown in Fig. 9 for the example helicopter with ground impact velocity at the critical speed. The behavior described above can be seen in the snapshots, and in the time history of the vertical motion and force experienced by the fuselage, shown in Figs. 10 and 11. Notice that the acceleration rapidly increases on initial impact, but the subsequent stroke of the landing gear acts to reduce this value by providing a smaller acceleration over a longer period of time. The maximum acceleration and force that occur at initial impact are the important quantities of interest (Figs. 10 and 11).

3.3 Typical Hard Landing With General Aircraft Orientation.

A typical, hard landing in which the aircraft has a general orientation is more complex. Several phases can be identified during the landing: (1) Free fall; (2) Initial Impact; (3) Secondary Impacts; (4) Recoil; and (5) Oscillation and Settling. The main difference from a level landing occurs during initial impact and
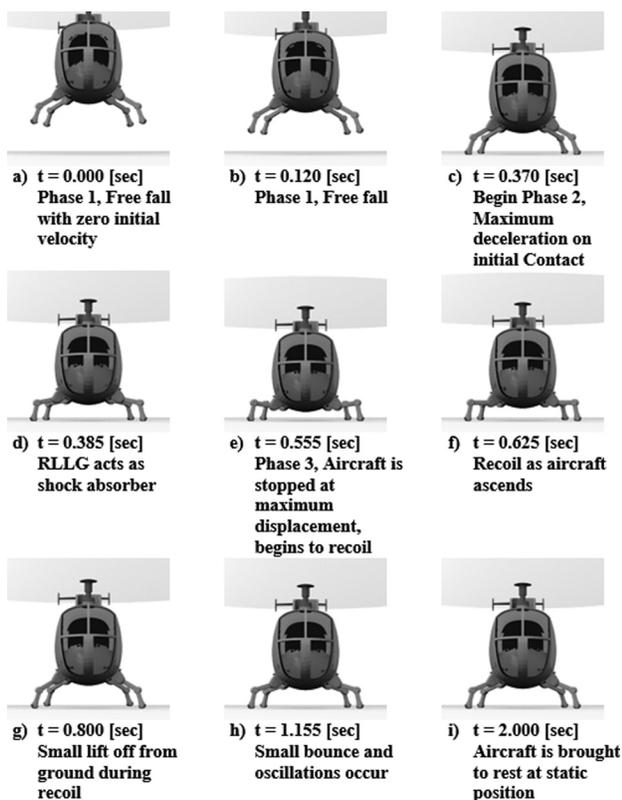
Fig. 9 Snapshots of a typical level hard landing simulation with the RLLG. The landing gear deflects during the impact, recoils, oscillates, and settles to its static, final position. (*a*) *t* = 0.000 (s) Phase 1, free fall with zero initial velocity; (*b*) *t* = 0.120 (s) Phase 1, free fall; (*c*) *t* = 0.370 (s) begin Phase 2, Maximum deceleration on initial contact; (*d*) *t* = 0.385 (s) RLLG acts as shock absorber; (*e*) *t* = 0.555 (s) Phase 3, aircraft is stopped at maximum displacement, begins to recoil; (*f*) *t* = 0.625 (s) recoil as aircraft ascends; (*g*) *t* = 0.800 (s) small lift off from ground during recoil; (*h*) *t* = 1.155 (s) small bounce and oscillations occur; and (*i*) *t* = 2.000 (s) aircraft is brought to rest at static position.
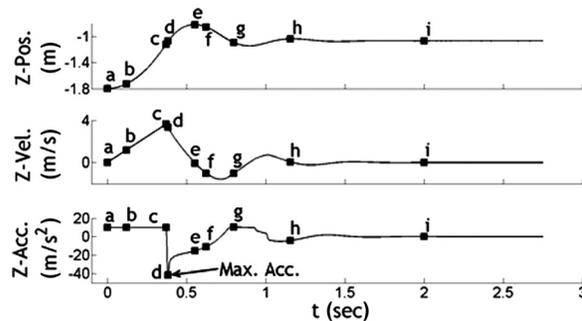
Fig. 10 Time history of the vertical motion of the fuselage mass center for the hard landing simulation shown in Fig. 9

deceleration. Depending on the orientation, one or several legs make contact during initial impact. Then, as the aircraft rotates, other legs make contact. This results in an initial impact and several secondary impacts. The peak deceleration may occur during any one of these impacts, depending on several factors, including weight of the aircraft, impact speed, initial leg angles, and initial orientation of the aircraft. Additionally, the recoil phase involves rocking of the aircraft as it pitches and/or rolls back and forth.

An additional, important characteristic of these types of landings is the significance of the angular acceleration and moments experienced by the vehicle. These situations involve much larger angular acceleration and associated larger moments. The angular acceleration time history is typically similar to the translational acceleration. It is characterized by an initial peak during initial impact and additional peaks during the secondary impacts and recoiling of the aircraft. Moments applied to the fuselage by the landing gear behave similarly.

3.4 Development of Landing Gear Configurations.

The joint stiffness and damping in the RLLG provide shock absorption during impact. Stiffness and damping coefficients are used to control leg angles and stroke during a landing event. With respect to these coefficients, two landing gear configurations were considered: conventional landing gear and actively controlled RLLG landing gear. The conventional configuration is a high stiffness system representing the dynamic behavior of traditional skid gear. The active configuration described above uses feedback to compute desired stiffness and damping coefficients in the RLLG to achieve improved hard landing mitigation.

3.4.1 Conventional Configuration. The conventional landing gear model was based on the FEA simulations of a skid gear equipped aircraft during hard landings at the extreme points of the MIL-STD 1290 crashworthiness envelope [11] (see Fig. 12). MIL-1290 is the governing standard for crashworthiness of rotorcraft. Referring to Fig. 12, the following extreme points of the hard landing envelope were simulated via FEA: 10 deg roll impact
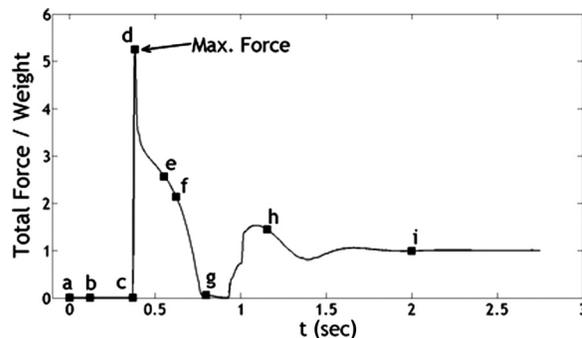
Fig. 11 Time history of the total force transmitted to the fuselage through the RLLG for the simulation shown in Fig. 9

at 10 ft/s, −5 deg pitch impact at 10 ft/s, 15 deg pitch impact at 10 ft/s, and level impact at 10 ft/s.

The conventional model was defined by setting the stiffness and damping coefficients in the RLLG joints so that the motion of the fuselage mass center for the multibody simulations matched reasonably well with the FEA simulation cases listed above. For example, Figs. 13 and 14 show comparisons of the mass center's vertical motion for the multibody simulation and the FEA simulation for the 10 deg roll and level impact cases.

The conventional landing gear model still utilizes the RLLG model, but approximates the traditional, skid gear through the definition of the stiffness and damping coefficients in the joints of the landing gear. This approach was used as a baseline to compare with the actively controlled RLLG.

3.4.2 Active Configuration. The active configuration consists of the RLLG with control applied. The controller changes the RLLG's stiffness and damping coefficients according to Eqs. (21)–(24) to minimize the acceleration on impact. As an example of the open-loop implementation of the controller, consider the desired motion of the fuselage mass center during a landing event shown in Fig. 15. The positive z-acceleration is required to allow the fuselage to re-ascend to its final, static state. The trajectory for the acceleration was used to create a schedule for the joint parameters based on Eqs. (19)–(24). Typical results for a level landing are shown in Fig. 16. The motion of the fuselage mass center for conventional landing gear model is plotted in the figure for comparison. The controlled RLLG "flattens" the peak acceleration to a minimum value, producing a dramatic reduction in the maximum acceleration.

The closed-loop control gives similar results for level landings, but nonlevel landings can have a different initial impact if the legs bounce while in the parking brake control mode. Figure 17 shows a typical case, in which one or more of the legs bounced. This caused a large increase in damping to bring the leg(s) back into contact, resulting in the initial spike in acceleration before the transition to the hard landing control. After the aircraft has been stopped, the stiffness and damping are slowly restored to nominal, static values. This results in the slight oscillations toward the end of the landing.

4 Simulation Results and Parametric Trade Studies

The following parametric trade studies were performed in order to maximize the reduction in the peak acceleration experienced by the rotorcraft during hard landings. These trade studies were performed for the conventional and active landing gear
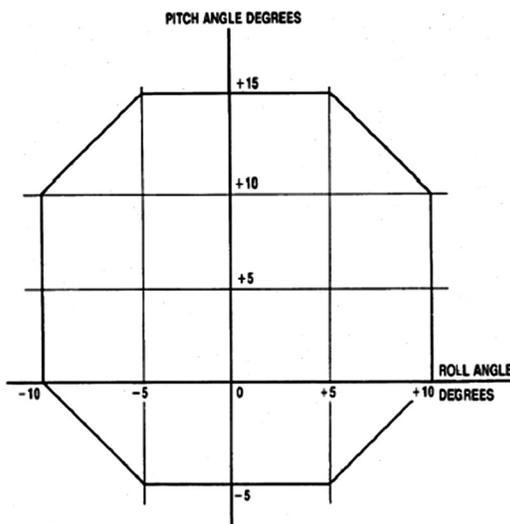
Fig. 12 MIL-1290 Crashworthiness envelope [11]
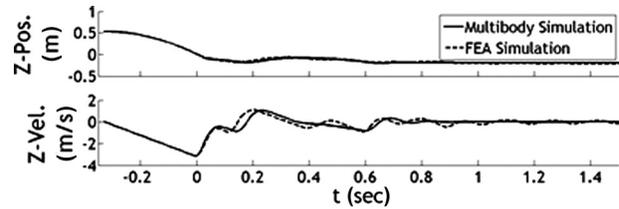
Fig. 13 The conventional landing gear model was refined until the fuselage mass center's vertical motion in the multibody simulation agreed reasonably well with the finite element model for the landing cases based on MIL-1290. The motion above is for the 10 deg Roll Impact.
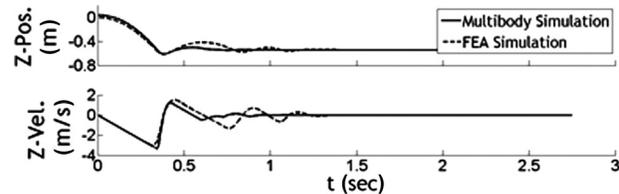
Fig. 14 Vertical motion of the fuselage mass center for level impact
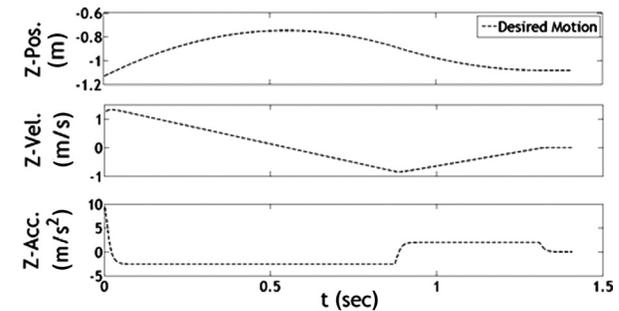
Fig. 15 Desired vertical, *z*-axis motion

configurations. For each study, the parameters were varied based on experience and ongoing work with the RLLG system.

4.1 Conventional Versus Active Configurations. Simulations of hard landings on level terrain were performed to contrast the active and conventional configurations of the RLLG. The open-loop control was used as the active configuration to simulate ideal, level landings. In these simulations, the nominal mass and dimensions shown in Figs. 7 and 8 were used. The initial angles were set to 60 deg and −10 deg for the upper and lower leg segments. The
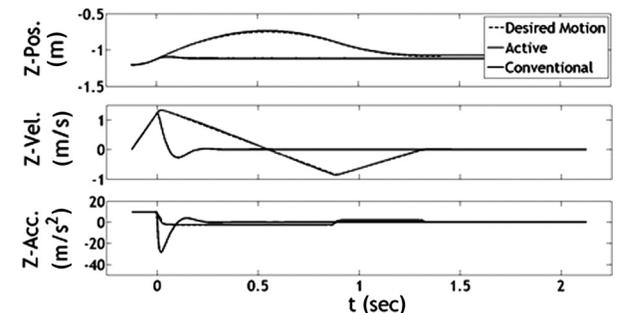
Fig. 16 Resulting vertical motion of the fuselage mass center during simulation with active control applied to the RLLG. Note that the active RLLG "flattens" the peak acceleration associated with the conventional gear.
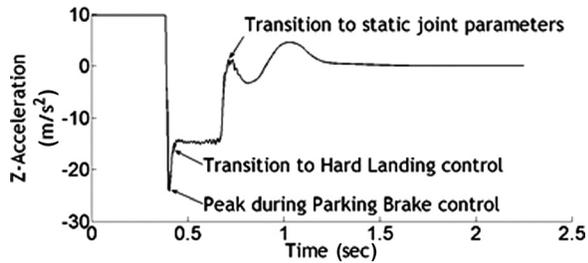
Fig. 17 Example of vertical acceleration versus time for closed-loop control for a nonlevel landing. The initial peak is due to the antibounce control operating during the parking brake mode, before all legs have touched the ground.

segment lengths were set to 0.46 m and 0.42 m (Fig. 8). These parameters along with the lengths of the leg segments and the initial leg segment angles are based on a previous research investigating landing capability, increased weight, and structural integrity of the RLLG. For the active configuration, the maximum deflection of the bottom of the fuselage was defined to be 75% of the nominal clearance, and the static deflection was defined as 10% of the nominal clearance. The desired z-acceleration was a continuous smooth function in time, similar to that shown in Fig. 15.

Impact speed was varied from approximately 33.3% to 100% of the critical speed. For each simulated landing event, the active, open-loop controller tracked the desired response accurately. The result is the "flattening" of the peak acceleration seen when the conventional configuration is used, similar to that shown in Fig. 16.

Figure 18 shows that applying active control to the joint stiffness and damping greatly reduces the maximum acceleration compared to a conventional landing gear system. In general, the maximum acceleration reduction was approximately 70% to 90%, depending on the impact speed.

4.2 Effect of Stance Width. In the previous simulated landing events, the leg segment angles provided a fair compromise between the stability of a wide leg stance and the stroke available to the landing gear (Fig. 19). The selected leg angles were 60 deg for the upper leg and −10 deg for the lower leg. These angles were varied to illustrate the effect of increasing the stroke. The angle of the upper leg was varied from 90 deg to 40 deg, while the angle of the lower leg was held constant at −10 deg. For each stance width, both the active and conventional configurations were tested for varying impact speeds (Fig. 20).

Conventional and active landing gear configurations follow opposite trends. For a narrow stance, the active RLLG has more travel available to the landing gear, allowing for a longer deceleration period. The conventional landing gear does not make use of
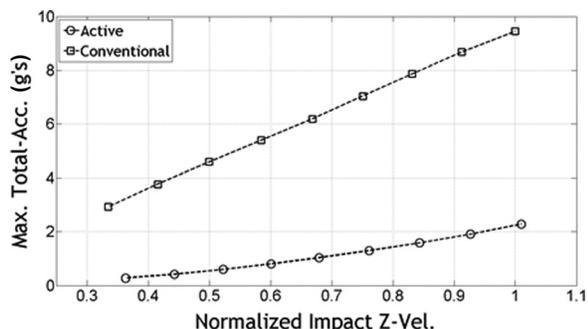
Fig. 18 Max acceleration versus impact speed for the conventional and active models. The active model generally reduces the acceleration by approximately 70–90%.

(a) Narrow Stance   (b) Wide Stance
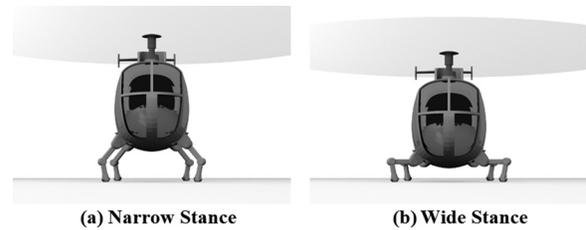
Fig. 19 A narrow stance (a) provides more distance through which the aircraft can decelerate compared to a wider stance (b)
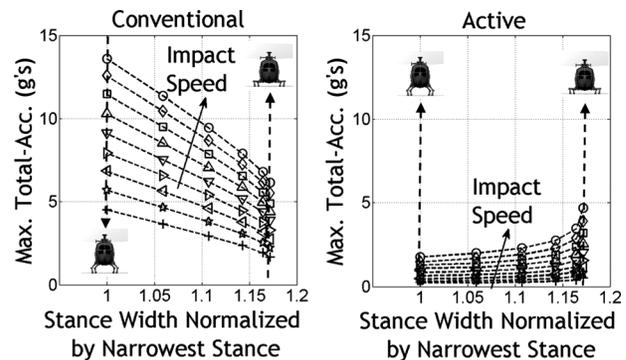
Fig. 20 Maximum acceleration versus stance width for the conventional landing gear and the active RLLG (right). Even at a large stance, the active model provides reduced acceleration. Note that opposite trends are seen in stance width, a larger stance width reduces acceleration for the conventional model and increases acceleration for the active model. The impact speed was varied from 33.3% to 100% of the critical speed.

the available travel. Therefore, the narrow stance causes a greater impulse to the conventional landing gear.

In both cases, initial leg angles have a significant effect. Referring to Fig. 20, the maximum acceleration can be changed by approximately a factor of two through the initial leg angles. Furthermore, since the conventional and active landing gear follow opposite trends, the benefit of the RLLG at narrower stances is increased. For example, Fig. 21 shows that the maximum acceleration of the active RLLG was less than 10% of that of the conventional landing gear for various impact speeds.

4.3 Effect of Maximum Dynamic Deflection. In the above results, the maximum deflection of the RLLG was set to approximately 75% of the nominal clearance with the ground. Increasing
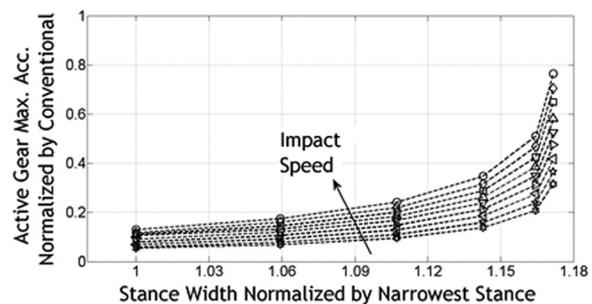
Fig. 21 Maximum acceleration with active RLLG as a percentage of the maximum acceleration with conventional gear for varying stance width. Note that even at wide stances, the RLLG still provides significantly smaller acceleration. The impact speed was varied from 33.3% to 100% of the critical speed.
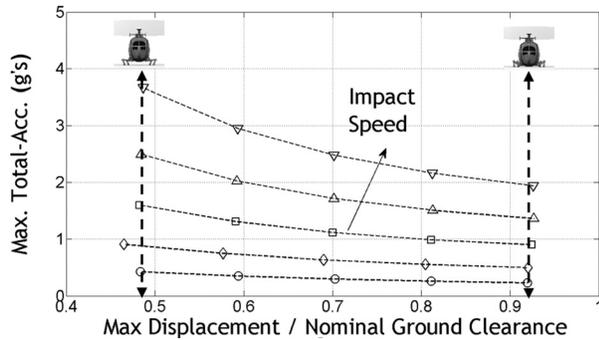
Fig. 22 Maximum acceleration versus maximum displacement of the RLLG during landing. Increasing the maximum deflection of the RLLG further improves the reduction in acceleration.

Table 1 Monte Carlo dispersed variables, based on normal probability distributions[a]

Parameter	Nominal, mean value	99% Confidence interval of normal dist. (3σ bounds)
Impact speed (ft/s)	12	[11.1, 12.9]
Mass (kg)	2050	[1896, 2204]
Pitch (deg)	0	[−6, 6]
Roll (deg)	0	[−6, 6]
Initial upper leg angles (deg)	60	[55.5, 64.5]
Initial lower leg angles (deg)	−10	[−10.75, −9.25]

[a]The aircraft was also given a random lateral velocity ranging from ±1 ft/s.
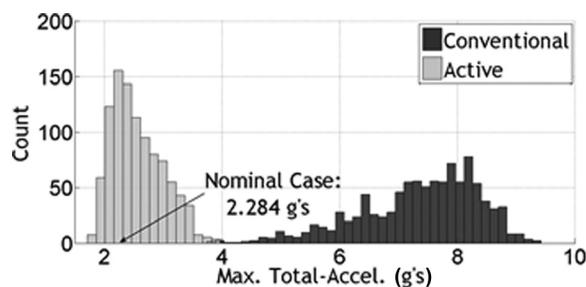
Fig. 23 Results of a 1000 run Monte Carlo simulation for the maximum acceleration of the fuselage mass center. The active RLLG maintains a distribution near the nominal case, providing robust control to plant variations, and a much smaller peak acceleration compared to the conventional case. The mean acceleration for the active RLLG is between 111% and 113% of the nominal value at a 95% confidence level.

the deflection provides another means of increasing the stroke and reducing the acceleration. To illustrate this effect, the maximum deflection was varied from approximately 50% to 90% of the nominal ground clearance. Initial leg angles were set to the nominal values of 60 deg and −10 deg for the upper and lower legs, respectively.

As shown in Fig. 22, the maximum acceleration of the active RLLG varied between 50% and under 10% that of the conventional landing gear. Even at a small travel of 50% of the nominal ground clearance, a significant reduction in the acceleration was realized. Furthermore, referring to the previous results, acceleration can be reduced further by using different initial leg angles (Fig. 20). With this in mind, it is reasonable to assert that the active model of the RLLG can provide 80% to over 90% reduction in maximum acceleration for a variety of level hard landings scenarios.

4.4 Robustness. The simulated landing events described so far involve a level landing in a controlled environment, in which all the parameters governing control of the RLLG are known exactly. The uncertainty associated with a real landing was simulated to test robustness of the RLLG controller to off-design conditions. The test involved a Monte Carlo simulation of 1000 simulated landing events. The parameters listed in Table 1 were varied randomly, based on a normal distribution. Each landing event simulated the nominal and level hard landing perturbed by variations of the parameters in Table 1. The Monte Carlo simulation was repeated for the closed-loop and open-loop controls with similar results. Closed-loop results are presented below.

Figure 23 shows the histogram for the maximum acceleration. The active RLLG provides a robust solution. The distribution is skewed toward the nominal maximum acceleration. For comparison, the conventional landing gear resulted in a wider distribution about a larger max acceleration. On average, the peak acceleration was 286% greater with the conventional landing gear than with the active landing gear. The mean and median of each distribution are shown in Table 2.

Additionally, the histogram of the maximum moment applied to the fuselage shows another benefit of the active RLLG. The moment under consideration is the total moment applied to the fuselage by the landing gear. As shown in Fig. 24, the active RLLG provided a smaller moment under variations in landing conditions. On average, the conventional landing gear provided a larger moment by about 166%. The histogram of the maximum force applied to a single-leg segment of the landing gear is shown in Fig. 25. Again, the active RLLG provided a smaller maximum force. The conventional landing gear provided a larger force by about 151%. The means and medians of the distributions are shown in Table 2.

4.5 Energy Transfer. In addition to reducing the acceleration during the hard landing, the RLLG provides an opportunity to harvest energy transferred during the landing. For example, consider a level landing at critical speed with the active RLLG. For this landing, the torques applied by the upper and lower joints are shown for the rear legs in Fig. 26. The torques assume nearly constant levels associated with each phase of the landing: descent, re-ascent to the static position, and the holding of the static position. Multiplying the torque by the angular rate of the corresponding leg segment and integrating in time gives the work done by the RLLG. This is shown in Fig. 27 for the rear legs.

The RLLG initially absorbs the energy of the impact. Then, a small amount of energy is used to return the fuselage to its static position. The difference between the energy used and the energy absorbed during impact represents the amount of energy available to be harvested. In this case, for a level landing at the critical

Table 2 Statistics for distributions shown in Figs. 23–25

| Variable | 95% Confidence interval of the mean | | Median | |
	Active	Conventional	Active	Conventional
Max acceleration [g's]	[2.5404, 2.5940]	[7.2792, 7.4064]	2.4813	7.5088
Max moment (normalized by mean value for Active case)	[0.9372, 1.0268]	[1.6358, 1.6796]	1.0073	1.6821
Max force on leg segment normalized by aircraft weight	[1.8137, 1.8553]	[2.7689, 2.7867]	1.7771	2.7782
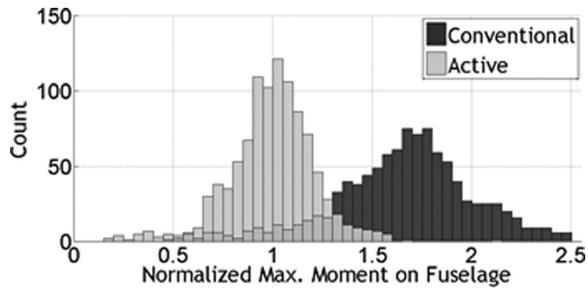
Fig. 24 Results of a 1000 run Monte Carlo simulation for the maximum moment applied to the fuselage. Again, the Active RLLG maintains a distribution around a smaller level than the conventional gear system. The moment was normalized by the mean value for the active RLLG.
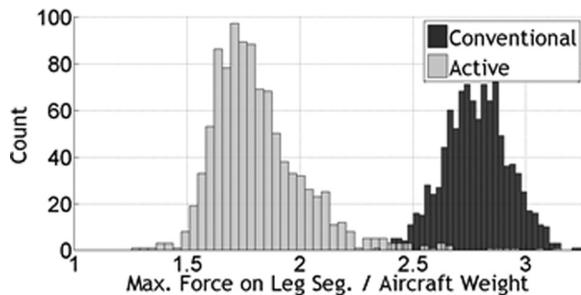
Fig. 25 Results of a 1000 run Monte Carlo simulation for the maximum force on an individual leg segment of the landing gear. Again, the active RLLG provided a significant reduction in force.
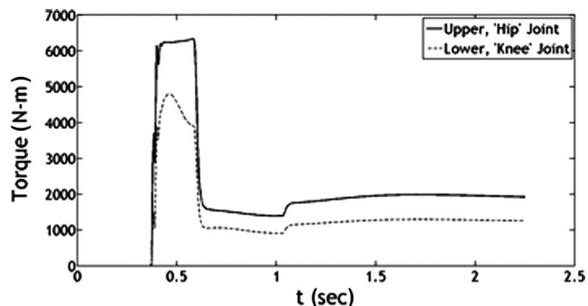
Fig. 26 Torque provided by the stiffness and damping in the rear legs for a level landing at the critical impact speed of 12 ft/s. The torque and angular rates are important design parameters for the actuation system. The simple profile shown above should be advantageous for different actuation schemes.

speed, the rear legs can provide approximately 4 kJ and 3 kJ for the upper and lower joints, respectively. Similarly, the front legs provide approximately 3 kJ and 2 kJ for the upper and lower joints. Adding the contribution of all joints gives a total of 24 kJ of energy to potentially be captured.

5 Conclusion

RLLG provides a powerful means to reduce loads on rotorcraft during hard landing events. The large stoke of the RLLG allows it to act as a shock absorber and reduce the force and acceleration caused by impact. The reduction in peak force and acceleration ranges from approximately 70% to 90% for level landing events. Similar reductions are seen for a variety of landing events that include roll and pitch angles, as well as small lateral velocities of
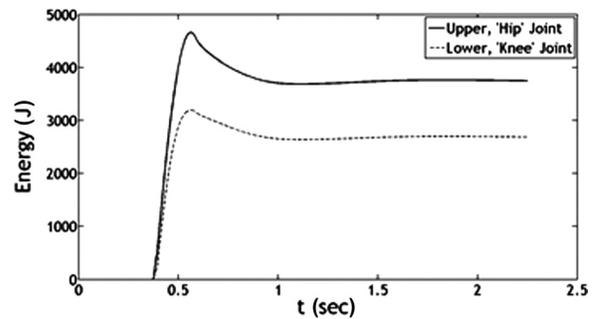
Fig. 27 Work done on the rear legs of the active RLLG. The initial rise occurs as the RLLG absorbs energy during impact. Then, after the aircraft reaches the bottom of its descent, the RLLG uses a small amount of energy to return the aircraft to its static position. This causes the decrease in energy occurring shortly after 0.5 s. The final, steady value for each joint represents the net energy that could potentially be captured for each joint.

the aircraft. These levels of reduction represent a great opportunity to enhance the landing capabilities and safety of rotorcraft. Equipping rotorcraft with the RLLG is practical, in terms of weight. Robotic landing gear adds a modest amount of weight to the system, as structure and actuators are required, but the additional weight is comparable to standard landing gear [30]. Furthermore, certain aircraft components can be designed to the lower loads seen with the RLLG system, yielding lower weight components. Thus, it is possible that an optimized aircraft could be lighter with the RLLG. The RLLG is also effective in a variety of configurations, including different stance widths, leg angles, and maximum tolerable deflections. The fact that the RLLG supports various configurations and effectively mitigates hard landings for a variety of landing conditions suggests that the device can widely be used for many aircraft with differing mission objectives.

Acknowledgment

Nomenclature

c_{in}, c_{it} = damping coefficients in normal and tangential directions for ith polyhedron in contact model ($N \times s/m$)

c_U, c_L = upper and lower leg segment damping coefficients ($N \times s/m$)

E_T, E_R = translation (m), rotational (rad) error components

f_f = ground friction force (N)

f_N = vertical force on a leg segment (N)

F_{TK}, F_{RK} = translation, rotational kinematic equations

F_{TD}, F_{RD} = translation, rotational dynamic equations

F_x, F_y, F_z = force measure numbers in body coordinates (N)

g = acceleration due to gravity, 9.81 (m/s^2)

G = constraint force and moment transformation matrix

I = mass moment of inertia matrix ($kg \times m^2$)

k_U, k_L = upper and lower leg segment spring coefficients (N/m)

k_{in}, k_{it} = spring coefficients in normal and tangential directions for ith polyhedron in contact model (N/m)

ℓ_U, ℓ_L = upper, lower lengths of leg segments

m = mass (kg)

M_x, M_y, M_z = moment measure numbers in body coordinates (N × m)

p, q, r = inertial angular rate measure numbers in body coordinates (rad/s)

q_0, q_1, q_2, q_3 = quaternion parameters describing orientation of body in inertial frame (nd)

R = proportionality constant between stiffness and damping coefficients (s)

$\vec{s}_{in}, \vec{s}_{it}$ = ith spring displacement in contact model in normal and tangential directions (m)

S_{ω_i} = skew symmetric cross product operator acting on angular rates

T_B = transformation matrix from inertial to body reference frame

u, v, w = inertial velocity vector measure numbers in body coordinates (m/s)

U = constraint force (N) and moment vector (N × m)

u_c = control input (desired acceleration) (m/s^2)

$\mathbf{u}_i$ = absolute velocity of contact point for ith polyhedron in the soft contact model

$\mathbf{w}_i$ = absolute velocity of surface element associated with the ith polyhedron in soft contact model

x, y, z = position vector measure numbers in inertial reference frame (m)

X = state vector

γ = pseudo control

ξ = damping ratio (nd)

θ_U, θ_L = upper, lower angles of leg segments with respect to vertical (rad)

ω_n = natural frequency (rad/s)

References

[1] Sharp, C. S., Shakernia, O., and Sastry, S. S., 2001, "A Vision System for Landing an Unmanned Aerial Vehicle," IEEE International Conference on Robotics and Automation, Seoul, South Korea, pp. 1720–1727.

[2] Sykora, B., 2009, "Rotorcraft Visual Situational Awareness, Solving the Pilotage Problem for Landing in Degraded Visual Environments," American Helicopter Society 65th Annual Forum, AHS, Ontario, CA.

[3] Taylor, T., 2009, "Rotorcraft Visual Situational Awareness (VSA): Solving the Pilotage Problem for Landing in Degraded Visual Environments," Proc. SPIE, **7328**, p. 73280G-1.

[4] Templeton, T., 2007, *Autonomous Vision-Based Rotorcraft Landing and Accurate Aerial Terrain Mapping in an Unknown Environment*, University of California at Berkeley, Berkeley, CA.

[5] Takahashi, M. D., Abershitz, A., Rubinets, R., and Whalley, M. S., 2013, "Evaluation of Safe Landing Area Determination Algorithms for Autonomous Rotorcraft Using Site Benchmarking," J. Am. Helicopter Soc., **58**(3), pp. 1–13.

[6] Coltman, J. W., Bolukbasi, A. O., and Laananen, D. H., 1985, *Analysis of Rotorcraft Crash Dynamics for Development of Improved Crashworthiness Design Criteria*, Simula, Inc., Tempe, AZ.

[7] Shanahan, D. F., and Mastroianni, G. R., 1984, "Spinal Injury in a U.S. Army Light Observation Helicopter," Aviat. Space Environ. Med., **55**(1), pp. 32–40.

[8] Iseler, L., and De Maio, J., 2002, *An Analysis of U.S. Civil Rotorcraft Accidents by Cost and Injury (1990–1996)*, National Aeronautics and Space Administration AMES Research Center, Moffett Field, CA.

[9] Couch, M., and Lindell, D., 2010, *Study on Rotorcraft Safety and Survivability*, Defense Acquisition University, Fort Belvoir, VA.

[10] Shanahan, D. F., 1993, *Basic Principles of Helicopter Crashworthiness*, Army Aeromedical Research Laboratory, Fort Rucker, AL.

[11] Standard Military, 1988, *MIL_STD_1290 (A) Light Fixed and Rotary-Wing Aircraft Crash Resistance*, Department of Defense, Washington, DC.

[12] Tho, C. H., Sparks, C. E., Sareen, A. K., Smith, M. R., and Johnson, C., 2004, "Efficient Helicopter Skid Landing Gear Dynamic Drop Simulation Using LS-DYN," J. Am. Helicopter Soc., **49**(4), pp. 483–492.

[13] Airoldi, A., and Lanzi, L., 2005, "Multi-Objective Genetic Optimization for Helicopter Skid Landing Gears," AIAA Paper No. 2005-2310.

[14] Chernoff, M., 1962, "Analysis and Design of Skid Gears for Level Landing," J. Am. Helicopter Soc., **7**(1), pp. 33–39.

[15] Stephens, B. E., and Evans, W. L., 1999, "Application of Skid Landing Gear Dynamic Drop Simulation," American Helicopter Society 55th Annual Forum, AHS, Montreal, Canada.

[16] Littell, J., 2011, "Full-Scale Crash Test of an MD-500 Helicopter," 67th American Helicopter Society Annual Forum, AHS, Virginia Beach, VA.

[17] Caprile, C., Airolid, A., and Janszen, G., 1999, "Multi-Body Simulation of a Helicopter Landing With Skid Landing Gear in Various Attitudes and Soil Conditions," 25th European Rotorcraft Forum, Rome, Italy, p. G-12.

[18] Kellas, S., Jackson, K. E., and Littell, J. D., 2010, "Full-Scale Crash Test of an MD-500 Helicopter With Deployable Energy Absorbers," American Helicopter Society 66th Annual Forum and Technology Display, AHS, Phoenix, AZ.

[19] Jackson, K. E., and Yvonne, T. F., 2008, "Comparison of ALE and SPH Simulations of Vertical Drop Tests of a Composite Fuselage Section Into Water," 10th International LS-DYNA Users Conference, Dearborn, MI, Document ID No. 20080022946.

[20] Kim, H., and Kirby, B. P. D., 2006, "Investigation of External Airbags for Rotorcraft Crashworthiness," J. Aircr., **43**(3), pp. 809–816.

[21] Airoldi, A., and Janszen, G., 2005, "A Design Solution for a Crashworthy Landing Gear With a New Triggering Mechanism for the Plastic Collapse of Metallic Tubes," Aerosp. Sci. Technol., **9**(5), pp. 445–455.

[22] Fagan, C. H., and Lynn, R. R., 1973, "Energy Absorbing Landing Gear," U.S. Patent No. 3,716,208, Feb. 13.

[23] Gentile, D. M., 1998, "Emergency Soft-Landing System for Rotor-Type Aircraft," U.S. Patent No. US5836544 A, Nov. 17.

[24] Logan, A. H., and Wagner, R. A., 1985, "For Use in an Aircraft," U.S. Patent No. US4519559 A, May 28.

[25] Mikulowski, G., and Holnicki-Szulc, J., 2004, "Adaptive Aircraft Shock Absorbers," Third European Conference on Structural Control, Jadwisin, Sept. 2–5.

[26] Sandy, D. F., and Furnes, K. M., 1999, "Energy Absorbing Landing Gear/Tail Skid," U.S. Patent No. US5927646 A, Jul. 27.

[27] Carter, Jr. J. W., 1999, "Crashworthy Landing Gear Shock," U.S. Patent No. US5944283 A, Aug. 31.

[28] Shwayder, W., 1985, "Helicopter Landing Skid Shoe Pad," U.S. Patent No. US4544116 A, Oct. 1.

[29] Smith, M. R., and Cheng-Ho Tho, S. C., 2011, "Crash Attenuation System for Aircraft," U.S. Patent No. US7954752 B2, Jun. 7.

[30] Manivannan, V., Langley, J. P., Costello, M. F., and Ruzzene, M., 2013, "Rotorcraft Slope Landings With Articulated Landing Gear," AIAA Paper No. 2013-5160.

[31] Leylek, E., Ward, M., and Costello, M., 2012, "Flight Dynamic Simulation for Multibody Aircraft Configurations," J. Guid. Control Dyn., **35**(6), pp. 1828–1842.

[32] Goyal, S., Pinson, E. N., and Sinden, F. W., 1994, "Simulation of Dynamics of Interacting Rigid Bodies Including Friction I: General Problem and Contact Model," Eng. Comput., **10**(3), pp. 162–174.

[33] Goyal, S., Pinson, E. N., and Sinden, F. W., 1994, "Simulation of Dynamics of Interacting Rigid Bodies Including Friction II: Software System Design and Implementation," Eng. Comput., **10**(3), pp. 175–195.

[34] 1990, Operators Manual: Helicopter, Observation OH-6A, Headquarters, Department of the Army.